Zhang *et al. Biochar* (2026) 8:99
https://doi.org/10.1007/s42773-026-00605-z

Biochar

ORIGINAL RESEARCH Open Access

Synergistic adsorptive reduction for enhanced U(VI) recovery from seawater via Fe_3S_4-decorated biochar nanosphere hybrids

Shijing Zhang[1], Shuang-Shuang Liu[2], Daiming Liu[3], Geyi Xu[1], Mengting Huang[1], Yuhui Zeng[1] and Si Luo[1*]

Abstract Herein, the in situ growth strategy successfully facilitated the synthesis of a novel BN-PDA@Fe_3S_4 composite through the integration of polydopamine-functionalized biochar nanospheres (BN-PDA) with Fe_3S_4. A suite of characterization techniques was employed to elucidate the microscopic morphology and crystallographic structure of the as-prepared adsorbent. Experimental results indicated that at 298 K and pH 5, the maximum U(VI) adsorption capacity of BN-PDA@Fe_3S_4 reached 203.4 mg g^{-1}, along with a remarkable improvement in the removal efficiency. The adsorption behavior of BN-PDA@Fe_3S_4 toward U(VI) was well described by the Langmuir isotherm model and Pseudo-second-order kinetic model, which confirmed the monolayer chemical adsorption nature of the process. Thermodynamic analyses further demonstrated that the U(VI) adsorption process was spontaneous and endothermic. Mechanistic investigations revealed that U(VI) ions could be reduced to less toxic U(IV) species, with this reduction process promoted by the reductive Fe(II) and S(-II) moieties in the Fe_3S_4 component. Collectively, this study provides a promising research avenue for the extraction of uranium from seawater.

Highlights

- A novel biochar nanosphere composite was successfully fabricated.
- U(VI) could be efficiently reduced to U(IV) by Fe(II) and S(–II).
- Fe_3S_4 and biochar nanosphere exhibited synergistic effects for U(VI) removal.
- Adsorption-reduction reaction served as a key mechanism for U(VI) removal.

Keywords Biochar nanospheres, Fe_3S_4, Adsorption, Reduction, U(VI)

*Correspondence:
Si Luo
Rose850101@163.com
Full list of author information is available at the end of the article

Springer

Graphic Abstract

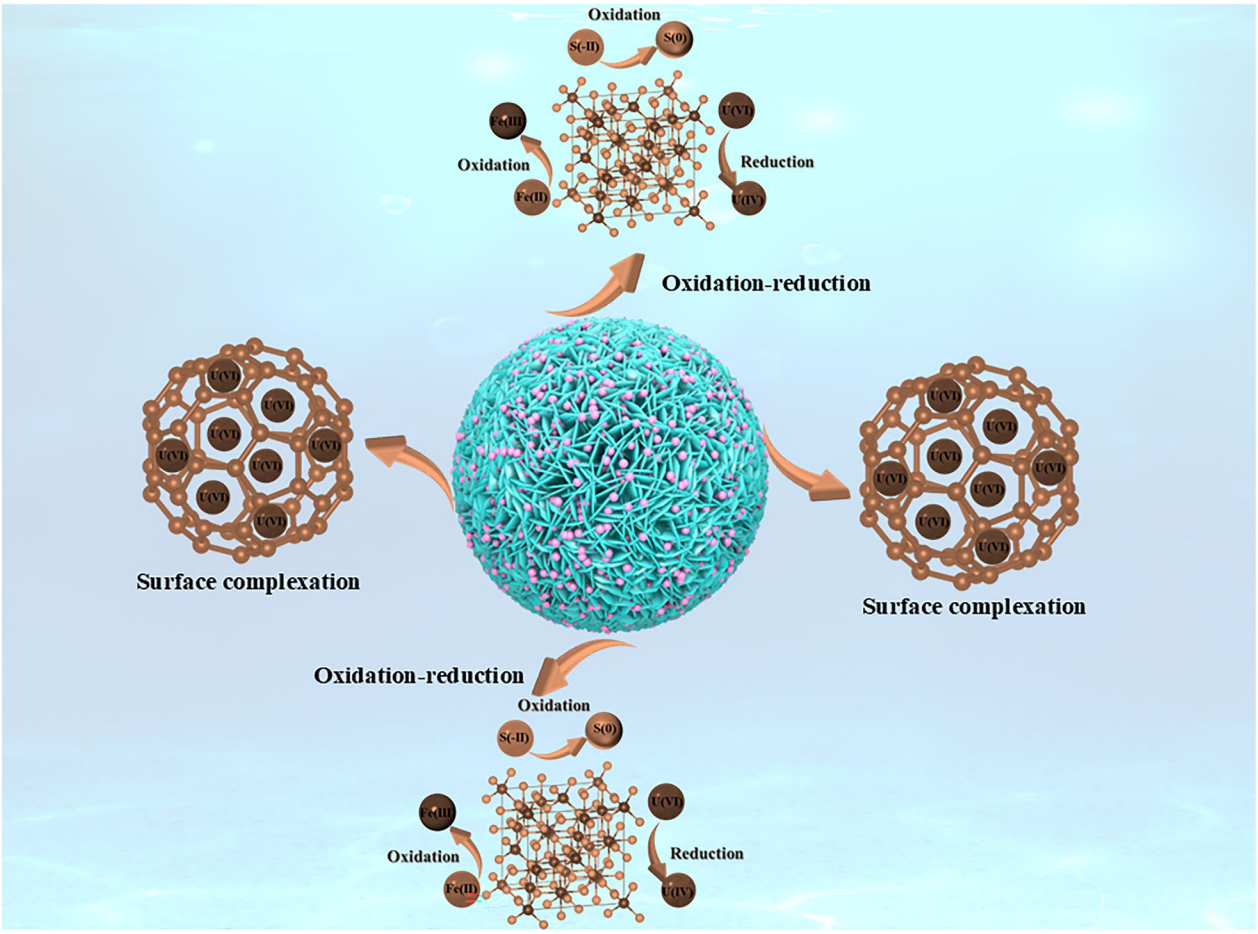

1 Introduction

Uranium is a critical nuclear fuel for the nuclear industry, with its global demand projected to maintain a long-term upward trend (Ahmed et al. 2021). Traditionally, uranium extraction from terrestrial ores has been challenging due to the uneven geographical distribution and limited reserves of uranium resources (Wei et al. 2025). It is reported that the total uranium reserves in seawater are roughly 1000 times those stored in terrestrial ores. Given this vast untapped resource potential, the development of efficient seawater uranium extraction technology is of profound strategic significance, particularly from the dual perspectives of sustainable nuclear energy development and environmental protection (Hu et al. 2026). To date, a wide range of technologies have been developed for the recovery of U(VI) from aqueous systems, including liquid–liquid extraction, chemical precipitation (Peng et al. 2025), electrochemical remediation, and adsorption (Han et al. 2023). Among these approaches, adsorption is broadly acknowledged as one of the most economically viable and practically implementable methods for the extraction of U(VI). Currently, traditional adsorbents used for U(VI) capture—such as MoS_2 (Ishag et al. 2023), polyaniline (Lei et al. 2018), nanomagnetite (Li et al. 2017), and fibers (Xiong et al. 2024) have undergone extensive research. Nevertheless, these materials possess inherent shortcomings: slow adsorption kinetics, limited maximum adsorption capacities, and the production of secondary waste. These limitations severely hinder their large-scale industrial application in nuclear wastewater remediation. Therefore, the rational design and manufacturing of advanced adsorbents endowed with excellent uranyl ion sequestration capabilities and strong resistance to harsh operating conditions, serve as a promising strategy to address the aforementioned challenges.

Biochar refers to a carbon-dense solid derived from the pyrolytic conversion of biomass under

oxygen-deficient environments (Chen et al. 2022). It possesses notable merits such as low manufacturing costs, extensive specific surface area, robust structural stability, and superior adsorptive capability (Guo et al. 2023a, b). To date, researchers have developed a diverse range of biochar-based composite materials for the remediation of uranium contamination, with promising outcomes being reported. For example, Zeng et al. (Xiong et al. 2024) fabricated an environmentally benign biochar doped with *Bacillus amyloliquefaciens*, which enabled efficient removal of U(VI) from aqueous solutions. Luo et al. (2025) employed phosphorylated chitosan-modified biochar to augment the adsorption capacity for high-concentration uranium(VI) in wastewater. Bai et al. (2025) reported the heterogeneous growth of ZIF-67 on water hyacinth-derived biochar and elucidated its efficient adsorption performance toward U(VI) in aqueous solutions. Xia et al. (2025) utilized phosphatized biochar derived from lychee shells for the removal of hexavalent uranium from mining wastewater. While these biochar-based materials exhibit favorable removal efficacy toward U(VI), they still suffer from limitations including low adsorption capacity, poor selectivity, and sluggish adsorption kinetics. Thus, the development of novel biochar-based materials is imperative.

As a distinctive morphological variant of biochar materials, biochar nanospheres exhibit core advantages in structural tunability, performance specificity, and application compatibility. Notably, they showcase greater potential than conventional bulk or powdered biochars across fields including adsorption, catalysis, and energy storage. Of particular significance, their spherical architecture endows them with robust mechanical stability, rendering them resistant to fragmentation under operations such as agitation or rinsing. This characteristic mitigates secondary contamination, facilitates recovery and reuse, and consequently reduces the associated application costs. Iron tetrasulfide (Fe_3S_4), an emerging adsorptive material, presents core strengths in adsorption applications, mainly including robust target-specific adsorption capacity, environmental compatibility, and reusability (Dong et al. 2025). Significantly, it shows superior performance in eliminating heavy metal ions and radionuclides—a feature that offsets the intrinsic limitations of traditional adsorbents, such as inadequate adsorption capacity, cumbersome recovery processes, and weak anti-interference capability. Furthermore, the introduction of amino functional groups onto the surface of biocarbon spheres not only enhances their hydrophilicity but also endows them with the capability to remove target pollutants. Based on the above analysis, a novel composite material was constructed by integrating the respective advantages of biochar nanospheres, Fe_3S_4, and amino functional groups, which is anticipated to address the challenge of radionuclide contamination.

Herein, a straightforward and eco-benign fabrication process was developed, which enabled the successful synthesis of a biochar-based composite (BN-PDA@Fe_3S_4) via a two-step synthetic strategy and its subsequent application in uranium separation and purification. To assess the composite's separation performance under varied conditions, comprehensive investigations were carried out. Notably, key parameters, such as solution pH, initial concentration, and reaction temperature, were systematically analyzed to determine their impacts on the material's uranium separation efficacy. Moreover, the separation mechanism was thoroughly explored and strictly confirmed by combining multiple spectroscopic analysis techniques, adsorption kinetic assessments, adsorption isotherm investigations, and other batch adsorption tests.

2 Materials and methods

2.1 Materials

The biochar nanospheres were obtained from Xi'an Qiyue Biotechnology Co., Ltd. The average particle size of the sample was determined to be 751.2 nm (Fig. S1), while its C and O contents were quantified as 97.18 at.% and 2.82 at.%, respectively (Table S1). The $Fe(NO_3)_3{\cdot}9H_2O$ (99.9%), thiourea (99%), ethylene glycol (99%), dopamine hydrochloride (98%), and $UO_2(NO_3)_2.6H_2O$ (99%) were purchased from Sigma-Aldrich. In all experiments, deionized water was used for dissolution.

2.2 Synthesis of the materials

The BN-PDA@Fe_3S_4 composite was synthesized with slight modifications based on the protocols described in references (Yang et al. 2014; Wu et al. 2023). First, 1 g of dopamine hydrochloride was dispersed in 300 mL of Tris-HCl buffer (pH = 8.6) under ultrasonic conditions. Then, 1.0 g of biochar nanospheres were added to the solution, which was maintained at 25 °C for 24 h. After that, the black precipitate was collected, followed by washing with deionized water and absolute ethanol to remove residual impurities, and then dried in a vacuum oven at 60 °C for 12 h to obtain the target product (BN-PDA). Second, 1.5 mmol of $FeCl_3{\cdot}6H_2O$, 3.0 mmol of thiourea, and 30 mL of ethylene glycol were added into 100 mL round-bottom flask. A preset mass of BN-PDA was added to the aforementioned solution afterward, followed by uniform dispersion via magnetic stirring. Thereafter, the well-dispersed mixture was transferred into a 100 mL autoclave and heated at 160 °C for 10 h. Once the hydrothermal process was completed, the obtained solid product was alternately rinsed with

absolute ethanol for several cycles. Ultimately, the rinsed product was subjected to vacuum drying at 60 °C for 12 h to remove residual moisture. After drying, the obtained final solid was named BN-PDA@Fe_3S_4.

2.3 Characterization

FTIR spectral analysis was performed using a Bruker TENSOR27 spectrometer over the range of 4000–400 cm^{-1} to characterize the functional groups. Field-emission scanning electron microscopy (FE-SEM, Netherlands) was employed to conduct the morphological analysis of the samples. N_2 adsorption/desorption experiment was performed using a Micromeritics (TriStar II Plus, America) instrument. X-ray photoelectron spectroscopy (XPS) analysis was performed using a PHI-5300 spectrometer with a normal Al Kα radiation. X-ray powder diffraction (XRD) patterns of the samples were acquired using a Philips X'Pert Pro Super diffractometer equipped with Cu Kα radiation.

2.4 Batch removal experiments

A batch technique was used to study the applicability of BN-PDA@Fe_3S_4 for adsorbing U(VI). An appropriate amount of $UO_2(NO_3)_2.6H_2O$ was first dissolved in deionized water with pH = 5 to prepare a 200 mg L^{-1} U(VI) stock solution. To maintain uniform experimental conditions, HCl and NaOH solutions were utilized to adjust the solution pH in all trials. A specified amount of adsorbent was added to a glass container holding 10 mL of U(VI) solution, and the mixture was then placed in a constant-temperature shaking incubator and continuously shaken at 200 rpm at room temperature for 24 h to achieve adsorption equilibrium. Upon completion of the adsorption equilibrium, solid–liquid separation of the adsorption mixture was performed via pressure filtration with a 0.45 μm mixed cellulose ester filter membrane. The concentration of remaining U(VI) in the filtrate was measured by a UV–Vis spectrophotometer at a wavelength of 651 nm. The effects of ion strength, initial concentration, contact time, and co-existing ions on U(VI) removal were also investigated. All experiments were repeated 3 times, and the results were expressed as mean ± standard deviation (Mean ± SD). It was worth noting that all adsorption experiments were conducted under a nitrogen atmosphere to preclude the oxidation of ferrous ions by dissolved oxygen. Besides, after reaching adsorption equilibrium, the used BN-PDA@Fe_3S_4 was magnetically separated, then re-dispersed into 30 mL of 0.5 mol L^{-1} Na_2CO_3 solution for 12 h. Subsequently, the sample was washed with a large amount of Milli-Q water and absolute ethanol three times each. The regenerated BN-PDA@Fe_3S_4 was used for the next adsorption cycle. Finally, the U(VI) removal rate and adsorption capacity of adsorbents were computed according to Eq. (1) and (2):

$$q_e = \frac{(C_o - C_e)V}{m} \tag{1}$$

$$R_e = \frac{C_o - C_e}{C_o} \times 100\%. \tag{2}$$

where C_0 along with C_e (mg L^{-1}) are the initial and equilibrium concentrations in clear liquor before and after sorption. V represented the volume of pollutant solution (L), and m is mass of samples (mg).

2.5 Statistical analysis

All batch removal experiments were conducted in triplicate, and the experimental data were expressed as the mean ± standard deviation (Mean ± SD). One-way analysis of variance (ANOVA) combined with Tukey's multiple comparison test was employed to identify the significant differences among experimental groups. A value of $^*p < 0.05$ was considered statistically significant, and $^*p < 0.01$ was defined as extremely statistically significant. All statistical computations and graphical plotting were performed using OriginPro 2023 (OriginLab Corporation, Northampton, MA, USA) and SPSS 26.0 software (IBM Corporation, Armonk, NY, USA).

3 Results and discussion

3.1 Structural characterizations

SEM images (Fig. 1) revealed that the BN exhibited a relatively uniform spherical morphology and a smooth surface. In contrast, the surface of BN-PDA became notably rough; this morphological change was primarily attributed to the coating of polydopamine on the BN surface. The morphology of Fe_3S_4 was characterized by a typical structure, consisting of a large quantity of 3D flower-like microspheres with uniform morphology. The morphology of BN-PDA@Fe_3S_4 was characterized by integrated spherical architectures and secondary nanostructured features. TEM characterization data further verified that both BN and BN-PDA possessed spherical architectures, while Fe_3S_4 showed a nanostructured configuration. Notably, the BN-PDA@Fe_3S_4 presented a typical morphological feature, in which spherical structures were evenly distributed on the surface of sheet-shaped architectures.

Meanwhile, as shown in Fig. S2, the elements S, Fe, N, O, and C were detected in the BN-PDA@Fe_3S_4 composite, which confirmed the presence of Fe_3S_4 in the composite materials. Figure 2a reveals that unlike pristine BN, the BN-PDA exhibited a distinct amino group absorption

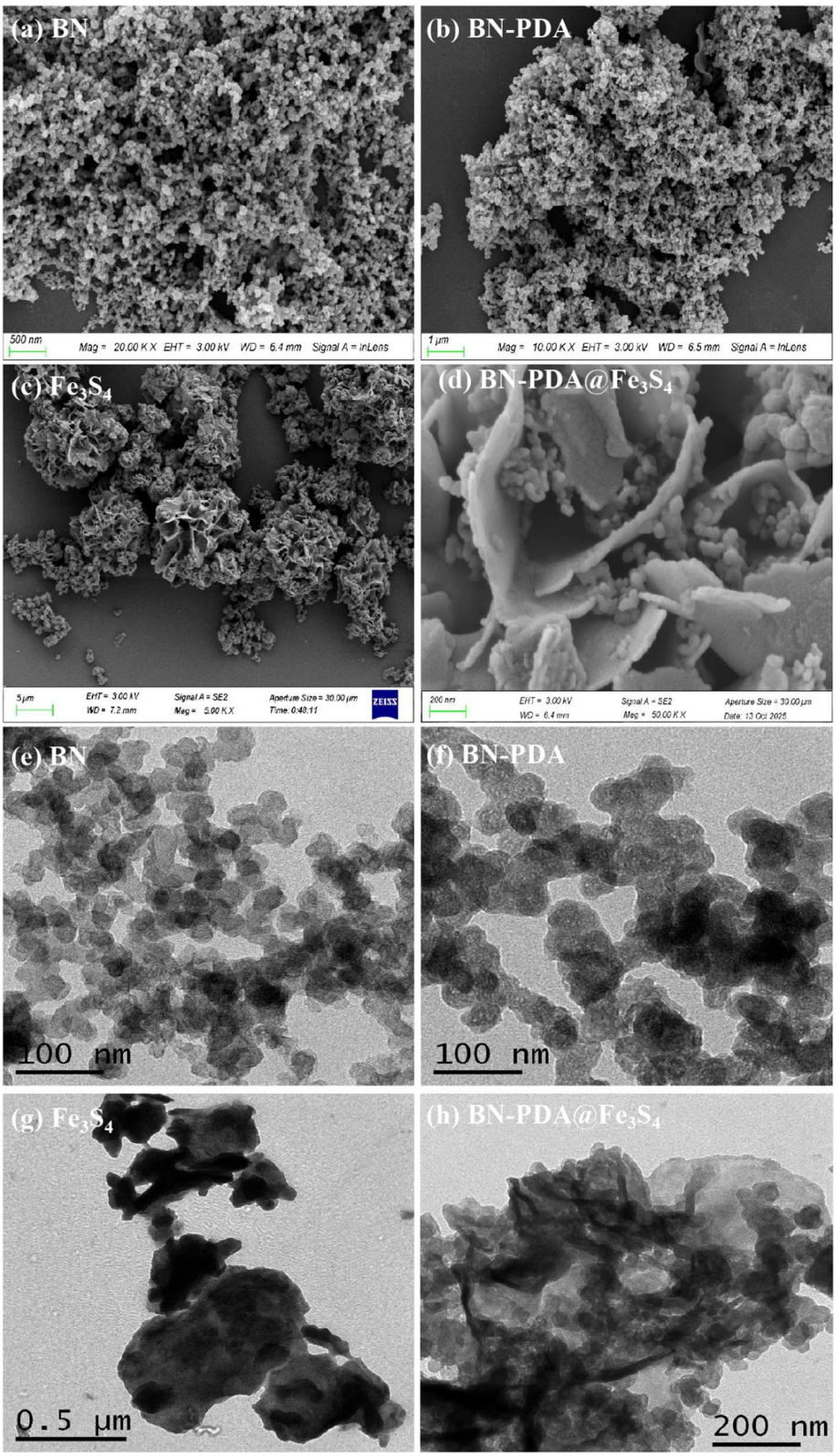

Fig. 1 The SEM and TEM images of BN, BN-PDA, Fe_3S_4, and BN-PDA@Fe_3S_4

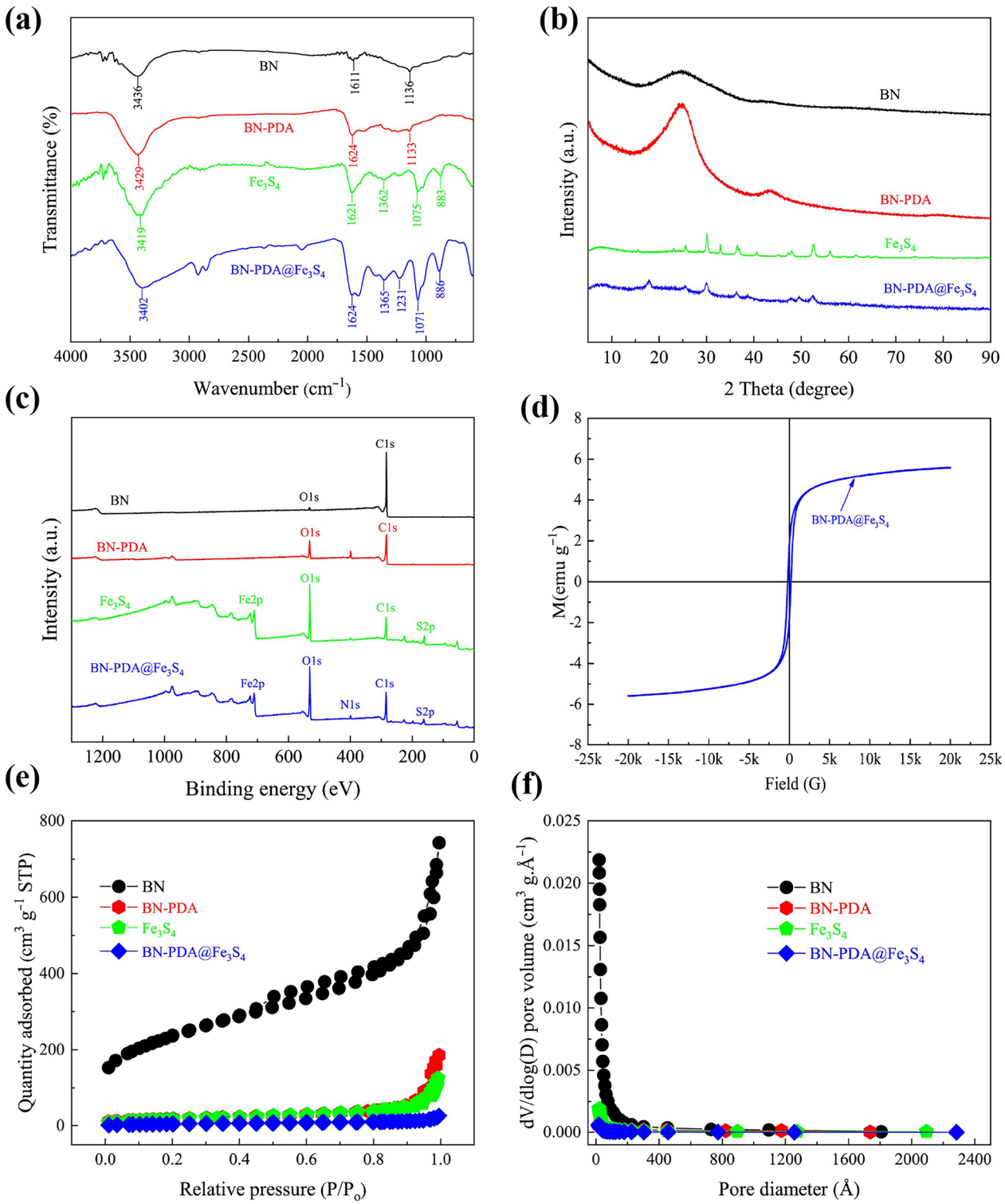

Fig. 2 The FTIR spectrum, XRD pattern, XPS survey spectra, magnetization hysteresis curves, N_2 adsorption–desorption curves and pore size distribution of BN, BN-PDA, Fe_3S_4 and BN-PDA@Fe_3S_4

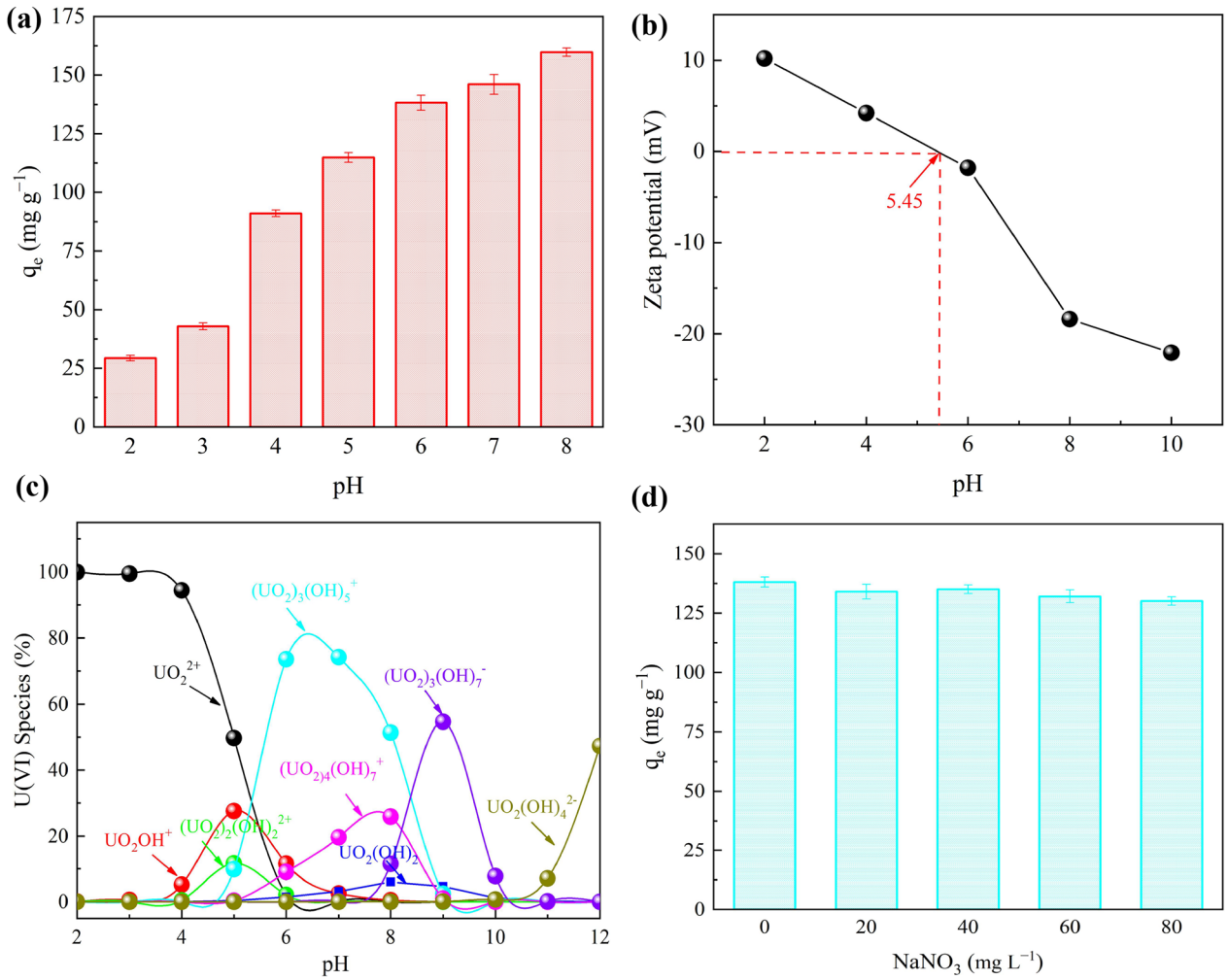

Fig. 3 **a** Effect of pH on U(VI) adsorption capacity; **b** Zeta potential of BN-PDA@Fe_3S_4 as a function of pH; **c** Dispersion behavior of U(VI) in aqueous solutions under different pH conditions; **d** Influence of ionic strength on U(VI) adsorption capacity

peak at 1624 cm^{-1}, which provided direct evidence for the successful anchoring of PDA on BN (Zhang et al. 2024). For Fe_3S_4, well-defined absorption bands for O–H, S–O, and Fe–O groups were detected at 3428, 1075, and 883 cm^{-1} (Yang et al. 2019), respectively. Notably, BN-PDA@Fe_3S_4 showed typical bands of both Fe_3S_4 and BN-PDA, verifying BN-PDA's successful immobilization onto Fe_3S_4. Figure 2b shows that the XRD characteristic peaks of the pristine BN and BN-PDA were consistent with each other. Pure Fe_3S_4 exhibited distinct diffraction peaks at 2θ values of 15.6, 25.6, 30.1, 33.0, 36.6, 40.6, 47.9, and 52.7°, which confirmed that Fe_3S_4 possesses a well-defined crystalline structure. However, BN-PDA@Fe_3S_4 showed diffraction peaks at 2θ = 17.8, 25.6, 29.8, 36.2, 48.1, and 52.5°, indicating the coexistence of both BN-PDA and Fe_3S_4 phases in the composite.

XPS was employed to examine the surface chemical makeup of all specimens. As depicted in Fig. 2c, the as-prepared BN were primarily composed of C1s and O1s on their surface. On the other hand, the BN-PDA samples modified with polydopamine displayed an extra characteristic peak associated with N1s, a feature attributed to the effective anchoring of PDA molecules onto the BN surface. Of particular note, the complete XPS spectrum of the BN-PDA@Fe_3S_4 composite showed, alongside the characteristic peaks of O1s, C1s, and N1s, distinct signals corresponding to Fe2p and S2p. This finding served as direct evidence confirming that Fe_3S_4 had been successfully immobilized on the surface of BN-PDA. Figure 2d presents the magnetic hysteresis loops of the BN-PDA@Fe_3S_4 composite. The Ms value of BN-PDA@Fe_3S_4 decreased to 5.57 emu g^{-1}. This result implied that when exposed to an external magnetic field, BN-PDA@Fe_3S_4 was capable of achieving rapid and efficient separation from aqueous solutions, thereby facilitating the subsequent solid–liquid separation procedure. Besides, N_2

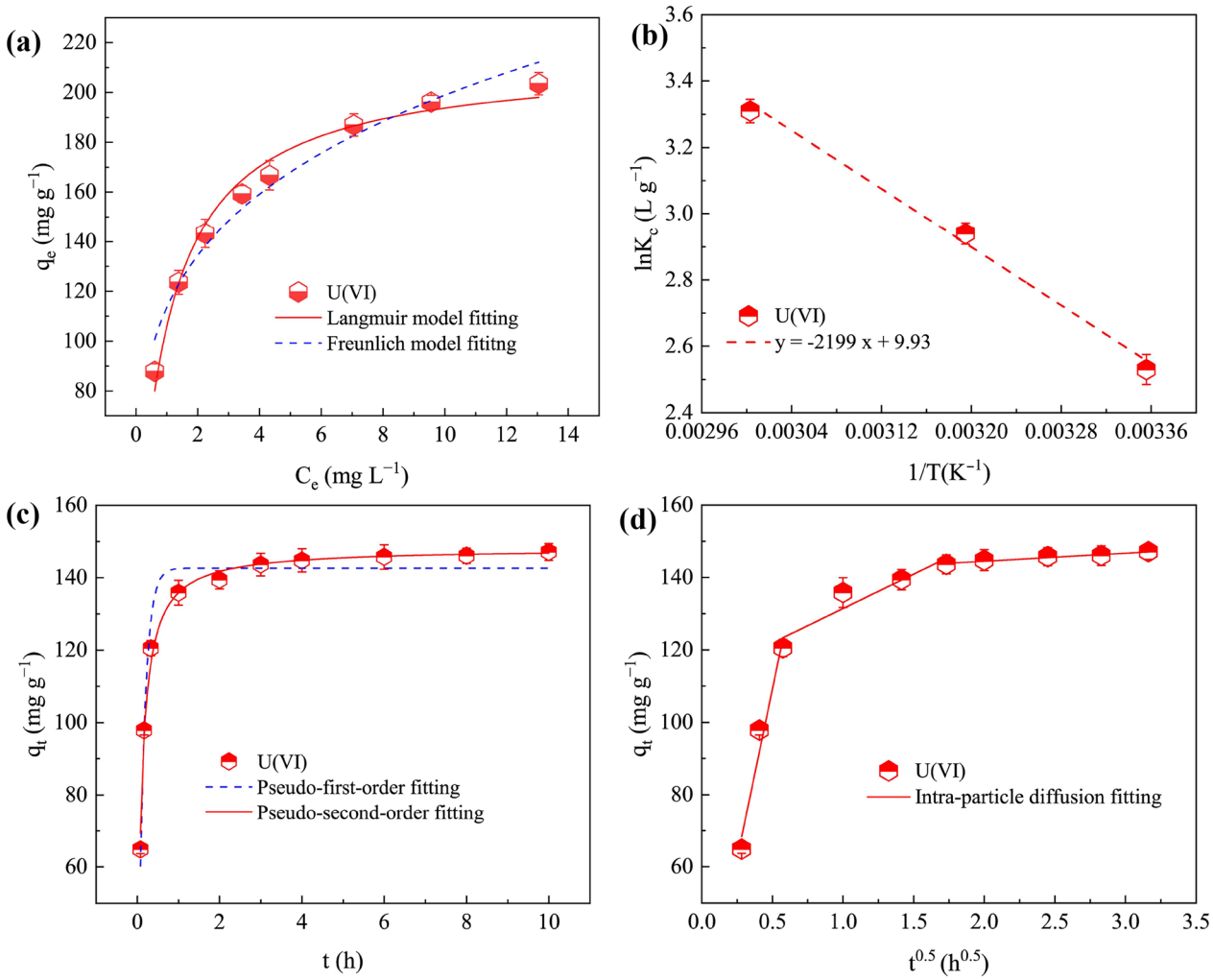

Fig. 4 **a** Langmuir and Freundlich models fitted results, **b** The liner plot of ln Kc versus 1/T, **c** Pseudo-first-order kinetic and pseudo-second-order kinetic fitted results, **d** Intraparticle diffusion model fitted results

adsorption–desorption measurements were further used to assess the specific surface areas of BN, BN-PDA, Fe_3S_4, and BN-PDA@Fe_3S_4. As depicted in Fig. 2e, f, all samples displayed classic Type IV isotherms with clear hysteresis loops—an indicator of ordered mesoporous structures that mirrored their pore formation characteristics. Calculations from Table S2 revealed their BET surface areas as 844.8, 70.1, 64.2, and 17.3 $m^2\ g^{-1}$ in sequence. Of note, the BN-PDA@Fe_3S_4 composite featured a more elaborate pore system and greater surface area. This structural benefit improved uranium ion accessibility and mobility, thereby enhancing its adsorption capability.

3.2 Effect of pH and ion strength

The pH of the solution played a pivotal role in determining both the speciation of metal ions within it and the adsorption capability of the adsorbent. As illustrated in Fig. 3a, the efficiency of U(VI) removal varied across different pH levels. Specifically, when the pH value ranged from 2 to 6, the adsorption capacity of BN-PDA@Fe_3S_4 for U(VI) increased gradually. However, when the pH value exceeded 6, the further increase in adsorption capacity was attributed to the precipitation of U(VI). Figure 3b presents the zeta potential analysis, showing that BN-PDA@Fe_3S_4 acted as an anionic adsorbent when the pH was higher than 5.45. Meanwhile, Fig. 3c illustrates how uranium transformed into various species depending on pH conditions. Under low pH conditions, the adsorbent showed a weak ability to adsorb U(VI). This phenomenon was mainly due to the competitive adsorption effect between H^+ ions and UO_2^{2+} ions. Notably, as the pH continued to increase, the adsorption capacity for U(VI) improved correspondingly. This was because the protonation degree

of the adsorbent surface decreased, which enhanced its tendency to interact with UO_2^{2+} ions. However, when the pH rose further, the concentration of $(UO_2)^{2+}$ ions decreased markedly. This reduction promoted the formation of more hydroxylated uranium species, and these species had a much lower binding affinity for the active sites of the adsorbent (Li et al. 2021). Figure 3d illustrates the influence of ionic strength on U(VI) removal efficiency. The study revealed that ionic strength exerted a relatively minor effect on the adsorption capacity of BN-PDA@Fe_3S_4, which supported the occurrence of inner-sphere complexation between uranyl ions and the adsorbent. This observation could be attributed to the low charge density and large ionic radius of Na^+; these characteristics promote strong interactions between Na^+ and surrounding water molecules, rather than competitive binding between Na^+ and the adsorbent's active sites. Furthermore, we also compared and examined the adsorption performance of uranium by four samples, namely BN, BN-PDA, Fe_3S_4, and BN-PDA@Fe_3S_4, under the same experimental conditions. As shown in Fig. S3, the experimental results showed that the adsorption performance of BN-PDA@Fe_3S_4 was significantly superior to the other three materials. This characteristic could be attributed to the synergistic effect between BN-PDA and Fe_3S_4.

3.3 Adsorption isotherm and kinetic analysis

Figure 4a illustrates the relationship between the adsorption capacity of BN-PDA@Fe_3S_4 for U(VI) and the equilibrium concentration. As the initial concentration of the U(VI) solution rose, the material's adsorption capacity first showed an increasing tendency; after the concentration hit a certain threshold, the adsorption capacity gradually leveled off. The core reason behind this behavior was that the number of active sites on the surface

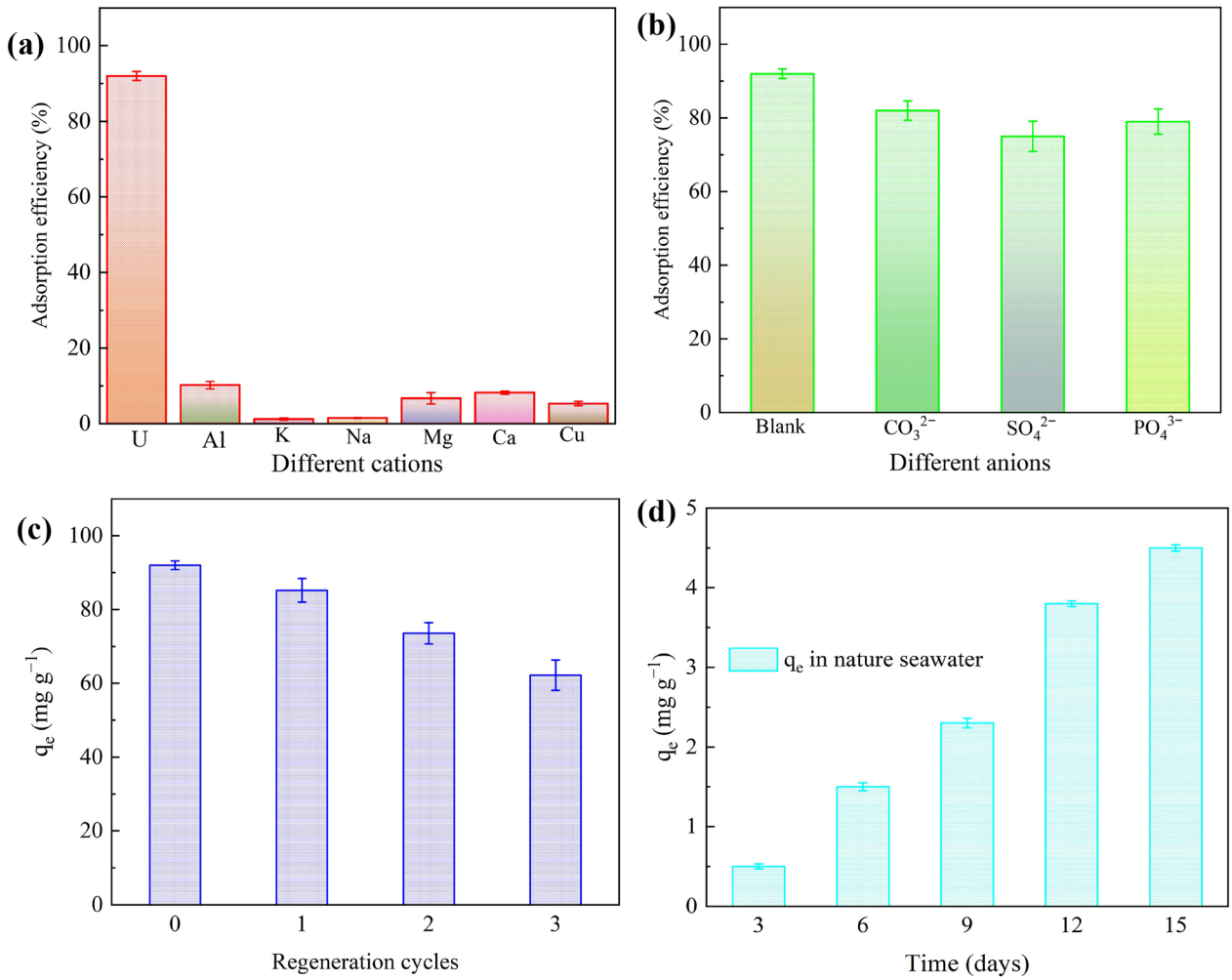

Fig. 5 **a** Effect of different cations on U(VI) adsorption capacity; **b** effect of different anionson U(VI) adsorption capacity; **c** recycling and regeneration performance of BN-PDA@Fe_3S_4; **d** recovery of U(VI) from nature seawater

of BN-PDA@Fe_3S_4-sites that could engage in specific interactions with U(VI) was restricted (Tian et al. 2023). When the U(VI) concentration in the solution was low, the active sites were not fully occupied, so the adsorption capacity went up as the U(VI) concentration increased. Once the surface active sites reached full saturation, even if the U(VI) concentration was raised further, the adsorption capacity did not undergo a noticeable change. Two classic adsorption isotherm models were further employed to fit the experimental data, aiming to systematically investigate the adsorption behaviors of U(VI). As illustrated in Fig. 4a and Table S3, the adsorption isotherm of the system exhibited a higher degree of fitting with the Langmuir model, which indicated that the adsorption of U(VI) onto the adsorbent follows a monolayer adsorption mechanism. Detailed thermodynamic parameters (ΔG^0, ΔH^0, ΔS^0) are presented in Fig. 4b and Table S4, all calculated through graphical analysis of experimental data. Negative ΔG^0 and positive ΔH^0 values confirmed that the adsorption of U(VI) onto BN-PDA@Fe_3S_4 was spontaneous and endothermic (Guo et al. 2025a, b). The positive ΔS^0 indicated increased disorder at the solid–liquid interface during adsorption (Zhang et al. 2025). As summarized in Table S5, the BN-PDA@Fe_3S_4 composite demonstrated a distinct superiority in U(VI) adsorption capacity compared to the previously reported adsorbents. This enhanced performance was primarily ascribed to the synergistic interaction between PDA and Fe_3S_4. Specifically, the functional groups of PDA could compensate for the scarcity of polar coordination sites on Fe_3S_4, while the metal active sites of Fe_3S_4 could enhance the adsorption capacity for pollutants susceptible to interaction with metal ions, thereby increasing the total number of effective adsorption sites on the composite surface and enhancing the overall adsorption performance.

To further clarify how contact time affects the adsorption behavior, kinetic experiments were carried out at a pH of 5.0. As indicated in In Fig. 4c, the U(VI) adsorption capacity of all experimental systems rose sharply during the first 120 min of contact, and the entire adsorption process achieved equilibrium at the 240-min mark. The underlying reason for this trend is as follows: In the early phase of the contact process, the surface of BN-PDA@Fe_3S_4 was equipped with ample vacant active sites, which provided favorable conditions for the fast combination of U(VI) ions (Sun et al. 2025a, b). With the progression of adsorption, the accessible active sites on the adsorbent became gradually occupied, causing the adsorption rate to slow down steadily until the system reached a state of equilibrium. To clarify the adsorption mechanism of U(VI) on BN-PDA@Fe_3S_4, it was essential to determine the most suitable kinetic model. As shown in Table S6, the theoretical U(VI) adsorption capacity of BN-PDA@Fe_3S_4, calculated using the pseudo-second-order kinetic model, was in good agreement with the actual adsorption capacity obtained from experiments. Furthermore, the R^2 value of this model was higher than that of the other tested kinetic model. This result strongly verified that the adsorption rate was mainly controlled by the chemical reaction between U(VI) and the surface of BN-PDA@Fe_3S_4. Besides, the experimental data were further analyzed using the Weber-Morris model. As presented in Fig. 4d, the fitting line did not pass through the origin of the coordinate system, which indicated that intraparticle diffusion was not the sole rate-limiting step of the adsorption process, and that another mechanism may contribute to the overall adsorption behavior.

3.4 Adsorption selectivity and reusability

Considering that different interfering ions were capable of competing for active adsorption sites on the adsorbent, competitive adsorption tests were carried out to examine the impact of coexisting ions on BN-PDA@Fe_3S_4's U(VI) removal efficiency. The findings (Fig. 5a) revealed that Al, Ca and Mg ions impeded the removal of U(VI), while K(I) and Na(I) had little notable effect on U(VI) removal. The results indicated that cations with greater charge densities and larger hydrated ionic radii were prone to strongly attaching to the adsorbent's active sites; such attachment thus hindered the interaction between U(VI) and BN-PDA@Fe_3S_4. As presented in Fig. 5b, Cl^- and NO_3^- exerted a relatively negligible effect on BN-PDA@Fe_3S_4's U(VI) adsorption performance. However, CO_3^{2-} and SO_4^{2-} notably reduced its U(VI) adsorption efficiency. This phenomenon could be attributed to their ready formation of stable coordination complexes with U(VI) in solution; these complexes displayed weak affinity for the adsorbent surface, making them hard to be captured (Qian et al. 2014; Zhao et al. 2016). The recyclability evaluation of BN-PDA@Fe_3S_4 for U(VI) recovery was further conducted. Figure 5c shows that the adsorption capacity of the sample for U(VI) exhibited a consistent downward trend with an increasing number of regeneration cycles. The U(VI) adsorption capacity reduced from 92.0 mg g^{-1} to 62.2 mg g^{-1} after three adsorption–desorption cycles. This phenomenon could be primarily ascribed to the mild oxidation of lattice Fe^{2+} and S^{2-} species in Fe_3S_4, a sulfide with moderate reducibility, under ambient temperature. Such oxidation progressively accumulated with an increasing number of adsorption–desorption regeneration cycles, representing the dominant contributor to the deterioration in regeneration performance. Furthermore, the cumulative mild oxidation of Fe_3S_4 significantly compromised the regeneration stability of the composite. It continually

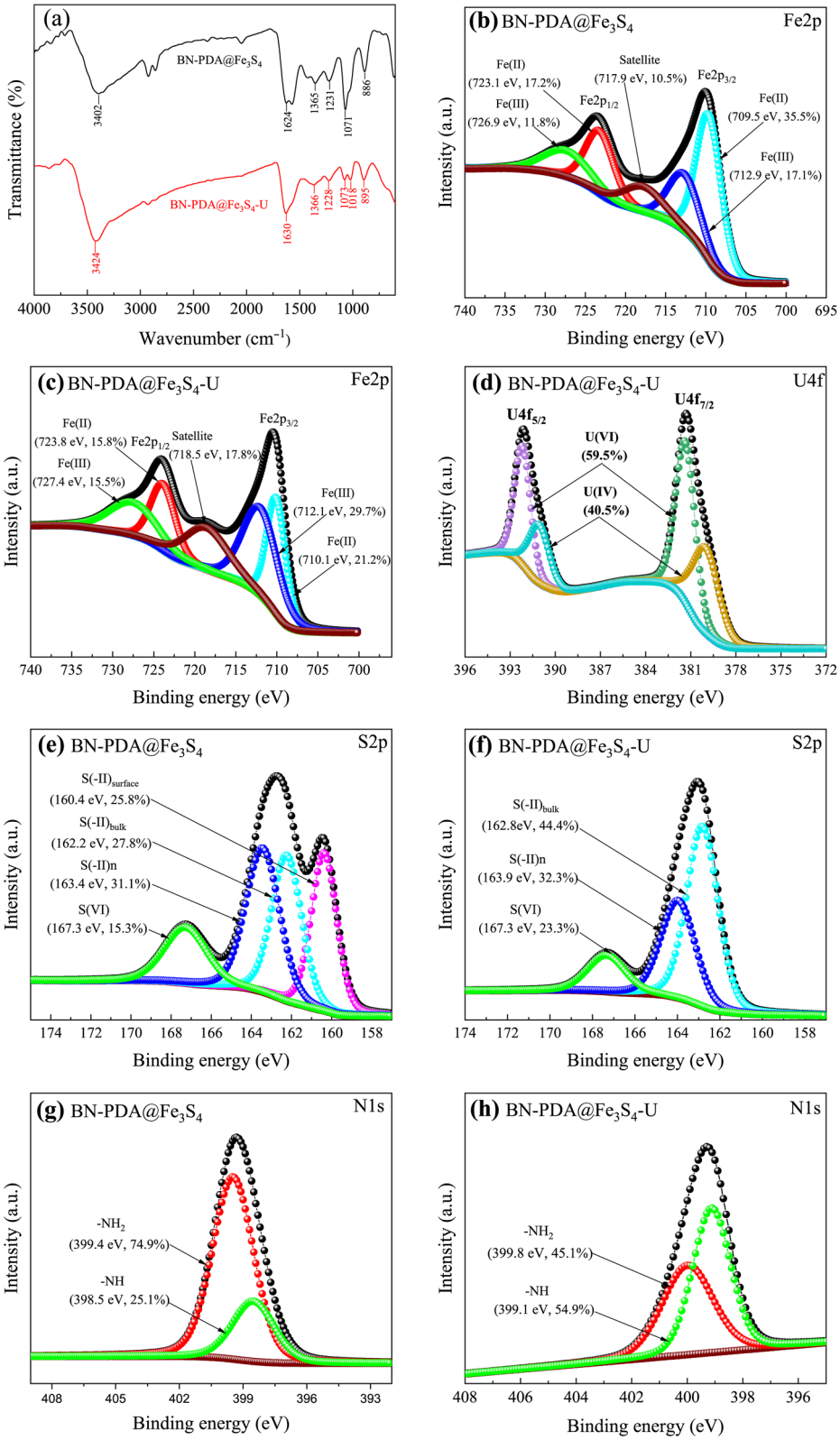

Fig. 6 **a** The FT-IR spectrum (**a**), high-resolution Fe2p (**b**, **c**), U4f (**d**), S2p (**e**, **f**) and N1s (**g**, **h**) of BN-PDA@Fe_3S_4 and BN-PDA@Fe_3S_4-U

depleted the Fe^{2+} and S^{2-} redox-active sites that mediated U(VI) adsorption and reduction, giving rise to a direct decline in cyclic adsorption–reduction capacity. Concurrently, oxidation-derived byproducts accumulated on the composite surface, impeding mass transport and further exacerbating the attenuation of performance. Natural seawater-borne microorganisms compromise adsorbent stability and adsorption performance over the long term by inducing biofouling. As illustrated in Fig. S4, the as-prepared BN-PDA@Fe_3S_4 achieved up to 90% antibacterial efficiency against *S. aureus* and *E. coli*, supporting its robust anti-biofouling capacity. Additionally, it is imperative to investigate the adsorption performance of BN-PDA@Fe_3S_4 in natural seawater. Figure 5d shows that BN-PDA@Fe_3S_4 still maintained its structural integrity after adsorbing in natural seawater for 15 days, with a uranium extraction capacity as high as 4.5 mg g^{-1}. We hypothesized that the exceptional performance of BN-PDA@Fe_3S_4 was attributed to the spatial cooperative effect among its adsorption sites. The rational spatial arrangement of the binding sites, along with their synergistic interactions, enabled the highly sensitive recognition of specific metal ions.

3.5 Removal mechanism

Different spectroscopic techniques were applied to characterize variations in the chemical speciation, morphological characteristics, and surface valence states of BN-PDA@Fe_3S_4 both prior to and following the reaction. As shown in Fig. 6a, when compared with the pristine BN-PDA@Fe_3S_4, the intensities of the characteristic S–O (1076 cm^{-1}) and Fe–O (606 cm^{-1}) peaks in the FTIR spectrum of BN-PDA@Fe_3S_4-U exhibited a distinct downward trend (Duan et al. 2018). Furthermore, the characteristic absorption peak at 2700–2900 cm^{-1} arose from the stretching vibration of saturated C–H bonds. After adsorption, the intensity of this peak decreased significantly, possibly because minor changes in the material's surface morphology and molecular conformation during adsorption caused some saturated C–H bonds to be covered or shielded by adsorbed molecules, reducing their effective contact with infrared light and thus weakening the peak intensity. Meanwhile, the weak absorption peak observed at 1018 cm^{-1} was mainly ascribed to the stretching vibration of the O=U=O functional group. Such spectroscopic evidence confirms that U(VI) species were effectively immobilized onto the surface of

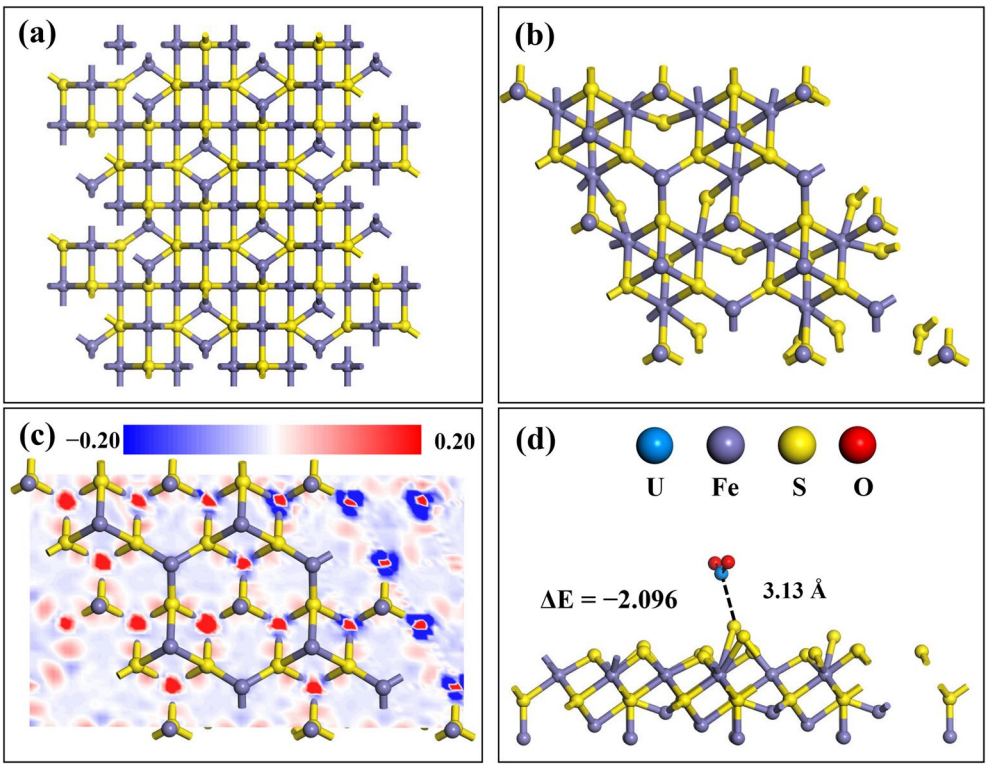

Fig. 7 **a** Crystal structure of Fe_3S_4; **b** Optimized structure of the Fe_3S_4 surface; **c** Charge density difference map of the Fe_3S_4 surface; **d** Optimized structure of compound U adsorbed on the Fe_3S_4 surface

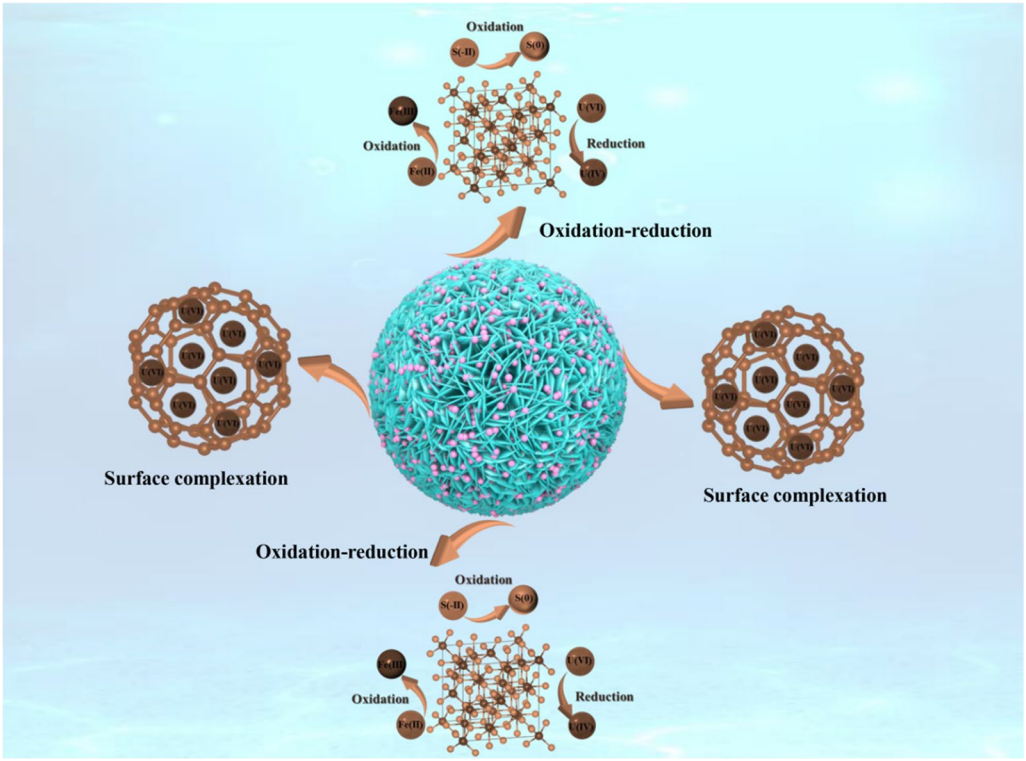

Fig. 8 The possible adsorption mechanism of U(VI) onto BN-PDA@Fe_3S_4

the adsorbents. Fig. S5 reveals that in the pristine adsorbent, the dominant elemental species corresponded to C1s, O1s, N1s, S2p and Fe2p, whereas a characteristic U4f peak emerged in the U(VI)-loaded BN-PDA@Fe_3S_4. Furthermore, the EDX results confirmed the presence of uranium on the surface of U-treated BN-PDA@Fe_3S_4, which consisted of C, O, N, S, Fe, and U elements. These experimental results further confirmed that uranium (U) had been successfully adsorbed onto the surface of the composite material.

XPS was utilized to examine variations in the chemical valence states of surface-associated elements within the samples prior to and following the reaction. Figure 6b displays the Fe2p spectra of the pristine BN-PDA@Fe_3S_4. In detail, the characteristic peaks associated with Fe(II) were situated at 709.5 eV and 723.1 eV, while the peaks detected at 712.9 eV and 726.9 eV were assigned to Fe(III). Furthermore, a satellite peak with notable intensity was identified at 717.9 eV. However, after the termination of the reaction, the relative content of Fe(II) in the BN-PDA@Fe_3S_4-U composite decreased from 52.7% to 37.0%, and the characteristic peaks corresponding to zero-valent iron (Fe^0) almost disappeared (Fig. 6c). These observations collectively implied that Fe (II) and Fe (0) served as the primary active sites for the reduction reaction. As illustrated in Fig. 6d, the U4f peak could be split into two separate sub-peaks, which were attributed to the $U4f_{7/2}$ and $U4f_{5/2}$ orbitals, respectively. Based on the U4f of Fe_3S_4@MBenes-U, the U(VI) characteristic photo-electron binding energy was observed at 381.5 and 392.2 eV, while the characteristic peak of U(IV) was centered at 380.1 and 391.1 eV. Meanwhile, quantitative analysis of the XPS spectra further revealed that the relative fraction of U(VI) species accounted for 59.5%, whereas that of U(IV) species was determined to be 40.5%. This result implied that a portion of U(VI) had experienced deoxygenation and been converted into uranium oxides or hydroxides deposits (UO_2, $UO_2(OH)_2$ and $(UO_2)_8O_2(OH)_{12}.12H_2O$) (Liao et al. 2025; Sun et al. 2025a, b). Figures 6e and f show the S2p spectra of BN-PDA@Fe_3S_4 and BN-PDA@Fe_3S_4-U. Notably, the characteristic signals of $S(-II)_{surface}$ and $S(-II)_{bulk}$ were centered at 160.4 eV and 162.2 eV, while the peaks at 163.4 eV and 167.3 eV were identified as $S(-II)_n$ and S(VI), respectively. However, after U(VI) removal, BN-PDA@Fe_3S_4-U lost all surface S(-II) species, with a concurrent increase in S(VI). This indicated that S(VI) was the major oxidation product of S(-II), and surface S(-II) was a key complexation site for U (VI). Figures 6g and h show the N1s spectra of BN-PDA@Fe_3S_4 and BN-PDA@Fe_3S_4-U. One could find that the relative percentages of $–NH_2$ and –NH on BN-PDA@Fe_3S_4 were 74.9% and 25.1%, respectively, whereas

those on BN-PDA@Fe_3S_4-U were altered to 45.1% and 54.9% after U(VI) adsorption. This change strongly suggested that amino groups were involved in mediating the adsorption process (Xiao et al. 2025; Guo et al. 2025a, b).

To clarify the structural and electronic properties of the Fe_3S_4 system, as well as its interfacial interaction mechanism with uranium, Fig. 7 summarizes key results from DFT calculations and structural characterizations. These findings confirmed that uranium species could form thermodynamically stable interactions with the Fe_3S_4 surface. Specifically, analysis of the charge density difference map revealed that the uneven charge distribution on the Fe_3S_4 (111) surface generated active sites favorable for uranium adsorption. The negative adsorption energy ($\Delta E = -2.096$ eV) further verified that this adsorption process was spontaneous and thermodynamically favorable. Meanwhile, the U–S bond length of 3.13 Å fell within the range of typical coordination bonds, indicating that uranium species were tightly bound to the Fe_3S_4 surface via chemical bonding. Collectively, these results provide a theoretical foundation for the application of Fe_3S_4 in solid-phase uranium immobilization or separation, and lay a basis for the subsequent design of structural modification strategies to develop high-efficiency uranium adsorbents. Drawing on the above analytical results, the potential uranium(VI) removal mechanism is depicted in Fig. 8. In the first stage, positively charged U(VI) species were drawn to the negatively charged surface of BN-PDA@Fe_3S_4 through electrostatic interactions; this process laid the foundation for the initial adsorption of U(VI) on the composite material. In the subsequent step, the adsorbed U(VI) was further converted to U(IV), a form with reduced toxicity, by the reductive moieties (Fe(II) and S^{2-}) that are inherently present in the Fe_3S_4 component of the composite.

4 Conclusion

In conclusion, a novel BN-PDA@Fe_3S_4 composite was successfully synthesized via a two-step method and subsequently applied to the removal of U(VI) from aqueous solutions. Static adsorption experiments demonstrated that the maximum U(VI) adsorption capacity of BN-PDA@Fe_3S_4 reached up to 203.4 mg g^{-1} at pH = 5.0 and 298 K. Meanwhile, the pseudo-second-order kinetic model and Langmuir isotherm model showed higher suitability for characterizing the U(VI) adsorption behavior of BN-PDA@Fe_3S_4. This finding demonstrated that the U(VI) removal process mediated by the composite material conforms to a monolayer chemisorption mechanism. Furthermore, BN-PDA@Fe_3S_4 displayed superior tolerance to coexisting ions and robust oxidation resistance. Mechanistic investigations revealed that U(VI) ions could be reduced to less toxic U(IV) species, with this reduction process promoted by the reductive Fe(II) and S(-II) moieties in the Fe_3S_4 component. Thus, BN-PDA@Fe_3S_4 exhibited considerable potential for practical application in uranium extraction from seawater.

Supplementary Information

The online version contains supplementary material available at https://doi.org/10.1007/s42773-026-00605-z.

Supplementary Material 1.

Acknowledgements
We would like to express our gratitude to the Hunan Agricultural University for its sponsorship.

Author contributions
Shijing Zhang: Writing- original draft preparation, Conceptualization, Investigation. Shuang-Shuang Liu: Methodology, Formal analysis, Investigation. Daiming Liu: Data curation, Software, Validation, Visualization. Geyi Xu: Validation, Formal analysis, Visualization. Mengting Huang: Methodology, Validation, Formal analysis. Yuhui Zeng: Methodology, Software, Investigation. Si Luo: Funding acquisition, Writing-review & editing, Supervision. All authors read and approved the final manuscript.

Funding
This research was supported by the National Key Research and Development Program of China (2022YFD1700102) and the Natural Science Foundation Project of Hunan Province (No. 2025JJ50193).

Data availability
All data generated or analyzed during this study are included in this article.

Declarations

Competing interests
The authors declare that they have no known competing financial interests or personal relationships that could have appeared to influence the work reported in this paper.

Author details
[1]School of Environment and Ecology, Hunan Agricultural University, Changsha 410128, People's Republic of China. [2]Guangdong Provincial Key Laboratory of Fishery Ecology and Environment, South China Sea Fisheries Research Institute, Chinese Academy of Fishery Sciences, Guangzhou 510300, China. [3]School of Mechanical Engineering, Sichuan University, Chengdu, China.

Received: 14 January 2026 Revised: 5 February 2026 Accepted: 25 February 2026
Published online: 08 May 2026

References

Ahmed W, Mehmood S, Ali S, Qaswar M, Shakoor A, Chen D (2021) Highly efficient uranium (VI) capture from aqueous solution by means of a hydroxyapatite-biochar nanocomposite: adsorption behavior and mechanism. Environ Res 201:111518

Bai H, Wang G, Liu J, Liu Y, Zhou J, Huang J (2025) Heterogeneous growth of ZIF-67 on water hyacinth biochar and its efficient adsorption performance for U(VI) in aqueous solution. Colloids Surf A Physicochem Eng Asp 714:136575

Chen W, Feng J, Liu S, Zhang J, Cai Y, Lv Z, Fang M, Tan X (2022) A green and economical MgO/biochar composite for the removal of U(VI) from aqueous solutions. Chem Eng Res des 180:391–401

Dong N, Ju J, Huang J, Du M, Wang L, Huang H, Li D, Xu F (2025) Photo-assisted Fenton degradation of tetracycline hydrochloride with magnetic Fe_3S_4/CuS composite. Appl Surf Sci 681:161581
Duan S, Xu X, Liu X, Wang Y, Hayat T, Alsaedi A, Meng Y, Li J (2018) Highly enhanced adsorption performance of U(VI) by non-thermal plasma modified magnetic Fe_3O_4 nanoparticles. J Colloid Interface Sci 513:92–103
Guo L, Peng L, Li J, Zhang W, Shi B (2023a) Highly efficient U(VI) capture from nuclear wastewater by an easily synthesized lignin-derived biochar: adsorption performance and mechanism. Environ Res 223:115416
Guo L, Lai X, Peng L, Li J, Zhang W, Shi B (2023b) Facile synthesis of Fe and N co-coped biochar from low temperature pyrolysis of lignin waste for superefficient Th(IV)/U(VI) separation: performance and mechanism. J Clean Prod 426:139168
Guo Q, Sun C, Li Y, Li K, Tai X (2025a) Novel poly(9-hydroxyfluorene)/NiO flower-like microspheres with good energy storage performance for supercapacitor application. Polymer 335:128833
Guo Q, Sun C, Li Y, Li K, Tai X (2025b) Recent advances of electrode materials applied in an electrochromic supercapacitor device. Molecules 30:182
Han Y, Xiong J, Zhang H, Chen X, Liu W, Chang Q, Li Q, Xie H, Qin Q, Li P (2023) Adsorption of low-concentrated U(VI) on a preferable crystalline boehmite (γ-AlOOH) in alkaline conditions. Ind Eng Chem Res 62:20802–20810
Hu B, Tai X, Wang X (2026) Hierarchical ransport channels break the mass-transfer bottleneck in seawater uranium adsorption. Sci China Chem. https://doi.org/10.1007/s40843-025-3919-0
Ishag A, Yue Y, Zhu W, Li C, Zhang B, Huang X, Sun Y (2023) The removal mechanism of U(VI) on nZVI/MoS_2 composites investigated by batch, spectroscopic, and modeling techniques. J Phys Chem C 127:15962–15968
Lei H, Pan N, Wang X, Zou H (2018) Facile synthesis of phytic acid impregnated polyaniline for enhanced U(VI) adsorption. J Chem Eng Data 63:3989–3997
Li M, Sun Y, Liu H, Chen T, Hayat T, Alharbi NS, Chen C (2017) Spectroscopic and modeling investigation of Eu(III)/U(VI) sorption on nanomagnetite from aqueous solutions. ACS Sustainable Chem Eng 5:5493–5502
Li Q, Chen Z, Wang H, Yang H, Wen T, Wang S, Hu B, Wang X (2021) Removal of organic compounds by nanoscale zero-valent iron and its composites. Sci Total Environ 792:148546
Liao Y, Shen C, Liu J, Yang M, Long J, Zhao J, Yu H, Wang M, Wang H (2025) Phytic acid-functionalized rGO/SnS_2 electrode composed of 2D/2D sandwich lamellas with multiple sites (P, O, S) for efficient long-term cyclic capture of U(VI). Chem Eng J 513:162721
Luo H, Xie S (2025) Mechanistic insights and performance evaluation of enhanced U(VI) capture by phosphorylated chitosan-functionalized biochar in aqueous systems. Mater Lett 391:138483
Peng W, He X, Chen X, Zhang Y, Yan C, Chen Z, Huang G (2025) Enhancement of U(VI) removal by g-C_3N_4/HAP composites via adsorption and solar driven photocatalysis synergy. J Water Process Eng 72:107584
Qian L, Ma M, Cheng D (2014) The effect of water chemistry on adsorption and desorption of U(VI) on nano-alumina. J Mol Liq 197:295–300
Sun Z, Chen Z, Tai X, Wang X (2025a) Uranium extraction from seawater: methods and challenges. Sci China Chem 68:9
Sun Z, Liao Y, Zhang Y, Sun S, Kan Q, Yu L, Dong Z, Wang Z, He R, Wang L, Meng Q, Wang H, Wang Q, Mao L, Pan D, Wang S, Zhang Z, Zhu W, Liu S, Wakeel M, Hu B, Duan T, Tai X, Wang X (2025b) Sustainable carbon materials in environmental and energy applications. Sustain Carbon Mater 1:7
Tian Y, Liu L, Wang Y, Ma F, Zhang C, Dong H (2023) Efficient removal of uranium (VI) from water by a hyper-cross-linked polymer adsorbent modified with polyethylenimine via phosphoramidate linkers. Environ Res 231:116160
Wei G, Chen Z, Tai X, Sun Z, Wang X (2025) Recent progress of uranium extraction and its catalytic applications. Trans Tianjin Univ 31:390–402
Wu A, Han M, Ding H, Rao H, Lu Z, Sun M, Wang Y, Chen Y, Zhang Y, Chen D (2023) Fe_3S_4 nanozyme inhibits tumor growth by synergistic effects of ferroptosis and apoptosis. Chem Eng J 474:145920
Xia Z, Zhang C, Chen X, Cai Y, Yi S, Liang R, Qiu J (2025) Phosphorylated litchi shell-derived biochar for removal U(VI) from mining wastewater. Chem Eng Sci 301:20708
Xiao M, Zhang X, Liu X, Chen Z, Tai X, Wang X (2025) Recent progress in covalent organic framework-based membranes: design, synthesis, and applications in the fields of energy and the environment. ACS Macro Lett 14:1201–1220
Xiong T, Zheng B, Li K, Zhang L, Zhang S (2024) Adsorption behaviors of U(VI) in aqueous solution by cetyltrimethylammonium bromide modified montmorillonite-hydroxyapatite composite adsorbent. Appl Clay Sci 262:107609
Yang H, Liao K, Huang H, Wu Q, Wan L, Xu Z (2014) Mussel-inspired modification of a polymer membrane for ultra-high water permeability and oil-in-water emulsion separation. J Mater Chem A 2:10225
Yang S, Li Q, Chen L, Chen Z, Pu Z, Wang H, Yu S, Hu B, Chen J, Wang X (2019) Ultrahigh sorption and reduction of Cr(VI) by two novel core-shell composites combined with Fe_3O_4 and MoS_2. J Hazard Mater 379:120797
Zhang H, Cheng S, Shen X, Pang Y (2024) Bimetallic MOF sulfurized In_2S_3/Fe_3S_4 for efficient photo-Fenton degradation of atrazine under weak sunlight: mechanism insight and degradation pathways. J Water Process Eng 68:106520
Zhang Y, Ma Q, Zhang H, Chen Z, Wang X, Lin Z, Xu F, Shao H, Zhang F, Fu D, Tai X, Yang H, Wang X (2025) Iodine doping covalent organic frameworks to reduce electron-hole recombination for promoting photocatalytic performance. Sci Bull. https://doi.org/10.1016/j.scib.2025.12.002
Zhao Y, Guo C, Fang H, Jiang J (2016) Competitive adsorption of Sr(II) and U(VI) on graphene oxide investigated by batch and modeling techniques. J Mol Liq 222:263–267